Sensors and Actuators B 254 (2018) 603–612

Contents lists available at ScienceDirect

Sensors and Actuators B: Chemical

journal homepage: www.elsevier.com/locate/snb

Au nanoparticles embedded in mesoporous ZrO_2 films: Multifunctional materials for electrochemical detection

Rusbel Coneo Rodríguez[a], Mariano M. Bruno[b], Paula C. Angelomé[a,*]

[a] Gerencia Química, Centro Atómico Constituyentes, Comisión Nacional de Energía Atómica, CONICET, Av. Gral. Paz 1499, San Martín, Buenos Aires, B1650KNA, Argentina
[b] Departamento de Química, Universidad Nacional de Río Cuarto, CONICET, Río Cuarto, X5804BYA, Argentina

ARTICLE INFO

Article history:
Received 8 February 2017
Received in revised form 11 July 2017
Accepted 12 July 2017
Available online 18 July 2017

Keywords:
Mesoporous thin film
Au nanoparticle
Composite material
Electrochemical sensor
Arsenic

ABSTRACT

Multifunctional electrodes that combine the adsorption capacity of mesoporous oxides and the electrocatalytic activity of metallic nanoparticles (NPs) were designed, synthesized and tested for As (III) determination in aqueous solution.

The electrodes were produced in two steps: first, mesoporous ZrO_2 thin films were prepared by evaporation induced self-assembly and, afterwards, Au NPs were included within the pores by adsorption of Au (III) and subsequent chemical reduction. Different pore sizes and Au NPs loadings were explored, in order to study its effect over the sensor's performance. The obtained materials were characterized by electron microscopy, UV–vis spectrometry and X Ray Reflectometry. The electrochemical performance was studied by cyclic voltammetry.

By comparison with empty ZrO_2 and Au loaded SiO_2 electrodes, it was possible to determine that the Au loaded ZrO_2 electrodes present a synergetic effect for the As (III) detection, combining the electrocatalytic behavior of Au NPs and the adsorption capacity of mesoporous ZrO_2. Moreover, a clear difference in the electrochemical performance of the material was observed depending on the pore size and the amount of incorporated Au NPs. In particular, a higher sensitivity (detection limit as low as 1.0 ppb of As (III)) was observed when small NPs (around 5 nm) were included within mesoporous films with bigger pore sizes (7 nm diameter) due to a higher accessibility.

1. Introduction

In the last decade, metallic nanoparticles (NPs) have attracted broad attention for their application in several fields. These applications are related to the size-dependent properties and the high surface to volume ratio of these nanomaterials. In particular gold NPs show excellent properties for numerous applications in the electrochemistry [1], electroanalytics [2,3] and bioelectrochemistry [4] fields, by providing an enhancement of mass transport and improving catalytic processes [5,6]. The most important feature concerning their superior electrochemical performance is their extremely high specific surface, that allows achieving high sensitivity using a small amount of material [7]. However, their response can be affected over time, due to electroactive area losing by leaching, coarsening and/or aggregation. Much effort has been devoted to solve these stability issues, being their dispersion into porous supports one of the most promising strategies. These supports provide anchoring sites to stabilize metal nanoparticles and help to maintain them well dispersed. Moreover, the NPs–support interface can play an active role in catalytic systems, by inducing an enhancement in the supported particles activity [8].

In that sense, ordered mesoporous oxides have received considerable attention as NPs supports, since they present controlled pore sizes and easily tunable framework's properties [9]. This tunability is a consequence of the synthetic method used to produce the mesoporous oxides: sol gel reactions to produce the framework, combined with amphiphilic molecules' self assembly to give rise to the mesopores. Interestingly, mesoporous materials can be deposited as thin films onto many substrates, expanding their possible applications [10]. In fact, mesoporous thin films (MTF) have been successfully used to design and fabricate chemically-modified electrodes, as summarized in recent reviews [9–11].

More importantly, the nanocomposites obtained through the combination of MTF and NPs posses not only the intrinsic properties of each component, but also new features derived from the synergy between them, mainly due to the high interfacial contact

---

* Corresponding author.
E-mail address: angelome@cnea.gov.ar (P.C. Angelomé).

http://dx.doi.org/10.1016/j.snb.2017.07.072
0925-4005/

area between the metal and the oxide [12]. In that sense, recently Au NPs dispersed into mesoporous mixed Zr-Ce oxides supports has been proposed by Violi *et al.* [8] as catalysts for a variety of chemical reactions, including electrochemical ones. In these electrodes, the Au NPs not only serve as reaction sites but also provide an electron pathway to the current collector as a string of pearls. In this work, a step further is presented: the use of a mesoporous oxide that acts both as a support for the Au NPs and as an adsorbent for the chosen analyte.

Arsenic (III) was chosen as the model analyte, since contamination with this species is a worldwide problem because of its notorious toxicity. The As (III) exposure, mainly through drinking water, can lead to various health problems involving the skin, lungs, urinary bladder or kidneys [13]. Arsenic (III) has been ranked by the International Agency for Research on Cancer (IARC) as a group 1 carcinogen [14]. Moreover, the World Health Organization (WHO) has fixed a maximum permissible concentration of 10 ppb for this contaminant in drinking water. Many analytical methods have been developed for determination of such levels of As (III) [15]. Electrochemical methods are the most suitable for in-field monitoring [16,17] due to their simplicity, low-cost, high speed and high sensitivity [18]. In particular, Au has been the most used electrode for As (III) detection, [19] because it shows excellent catalytic activity and good intrinsic conductivity [20]. In order to minimize the required amount of noble metal for the sensors construction, the use of Au NPs has been proposed in the last years [13]. Moreover, such Au NPs, supported onto different substrates, can influence the measurement performance, improving the sensitivity and detection limit for As (III) [13,21,22].

Mesoporous ZrO_2, on the other hand, has been chosen as the support oxide, as this oxide has been reported to be a good adsorbent for the removal of arsenic ions [23–25] and other pollutants from water [26]. In addition, ZrO_2 presents a high stability to harsh chemical environments, resulting ideal for the construction of highly durable devices.

Hence, in the present study, we propose the construction of composite electrodes: Au NPs included within the pores of ZrO_2 mesoporous thin films, for the detection of As (III) in aqueous solution. These electrodes combine the Au NPs electrocatalytic performance for the contaminant detection with the As (III) adsorption capability of mesoporous ZrO_2.

The oxide was obtained by Evaporation Induced Self Assembly (EISA) [27], using two different block copolymers as templates. The NPs deposition was performed by impregnation-reduction method, which presents several advantages over traditional methodologies, including:

(a) the Au NPs remain trapped inside the mesopores,
(b) no separate NPs preparation is required, resulting in a faster and greener methodology, since no organic solvents or toxic stabilizers are employed,
(c) the NPs surface is free from strongly bound capping agents, and
(d) a better distribution of NPs is obtained, when compared with electrodeposition procedures [8,28].

The effect of the Au NPs amount over the electrochemical detection of As (III) was evaluated and the composite's synergetic effect was confirmed by comparing with Au loaded mesoporous SiO_2 and non loaded mesoporous ZrO_2. The experimental results suggest that, when a careful control over the framework and Au NPs loading is achieved, the obtained modified electrodes show excellent performance for As (III) detection in neutral media.

Interestingly, the synthetic approach can be easily extended to the fabrication of other electrochemical sensors, by simply modifying the adsorbent mesoporous support.

2. Materials and methods

2.1. Materials

Zirconium *n*-propoxide in ethanol, acetylacetonate (acac), KOH, NaOH, diblock copolymer Brij 58 (B58), triblock copolymer Pluronic F127 (F127), tetraethoxysilane (TEOS), aminopropyltriethoxysilane (APTES), $HAuCl_4·3H_2O$, and sodium arsenite were purchased from Sigma-Aldrich. HCl 35% was purchased from Merck, absolute ethanol was purchased from Biopack and $NaBH_4$ was obtained from Riedel-de Haën. Water (resistivity = 18 MΩ) was obtained from an E-pure system. Bare glass, and indium-doped tin oxide coated glass (ITO, Delta Technologies) were used as substrates for film deposition.

2.2. Synthesis of sol-gel thin films

2.2.1. Preparation of the sols

Sols to give rise to mesoporous ZrO_2 were prepared following the procedure reported previously [29]. Briefly, acac, zirconium propoxide and the template (B58 or F127) were mixed in ethanol; the mixture was stirred for a minute. Then, HCl and water were added dropwise under vigorous stirring. The obtained solution, with molar ratio of 40 ethanol: 1 zirconium propoxide: 1 acac: 1 HCl: 20 H_2O: x template (with $x = 0.05$ for B58 and $x = 0.005$ for F127), was stirred for 1 h at room temperature before its use.

SiO_2 sols were prepared using TEOS as the oxide precursor and B58 or F127 as templates; the sols were prepared by mixing ethanol, TEOS, water and the copolymer, with the following the molar ratio:40: 1: 10 (HCl 0.004): x, where x was 0.05 for B58 and 0.005 for F127. This solution was aged for 24 h before the film deposition on the substrate [30].

2.2.2. Preparation of the films

Mesoporous thin films were produced by combining a sol−gel reactions with amphiphilic molecules self-assembly in the strategy known as Evaporation Induced Self Assembly (EISA) [27]. The films were prepared by dip-coating onto ITO coated glass substrates carefully cleaned with pure water and acetone, under 20–50% relative humidity (RH) and 20 °C. A withdrawal speed of 2.0 mms^{-1} was used in all cases. The as prepared films were transferred to a chamber with RH of 50% (obtained with a saturated solution of $Ca(NO_3)_2$) for 24 h. In order to remove the organic template and to promote a consolidation of the oxide structure, a gradual thermal treatment was applied. The heating procedure consist of three steps: 24 h at 60 °C, followed by 24 h at 130 °C and 2 h at 350 °C (heating rate 1 °C• min^{-1}). Before its use, the films were rinsed with water and ethanol and dried at 130 °C.

The ZrO_2 films obtained by using B58 and F127 as templates were denominated ZrB and ZrF, respectively. The same code was used for SiO_2 films, which were denominated SiB and SiF.

2.2.3. Infiltration with gold NPs

The infiltration of Au NPs on mesoporous films was achieved by an iterative adsorption/reduction (A/R) method based on previously reported procedures [8,31]. This methodology consists in the adsorption of a gold precursor onto the surface of the mesoporous oxide followed by a reduction with $NaBH_4$. In all cases, the film was immersed for one minute in 1 mM $HAuCl_4·3H_2O$ solution at pH = 4 (adjusted by adding 0.1 M NaOH solution). The pH was selected to promote the adsorption of the negatively charged Au(III) salt onto the positively charged surface of the film [31]. After this residence time, the film was rinsed and dried under air flow. Afterwards, it was immersed for 1 min in a 1 mM $NaBH_4$ solution, rinsed with water and dried under air flow. These two consecutive steps were repeated 8 and 15 times in order to achieve different degrees of NPs filling.

For ZrO_2 films, the adsorption of $AuCl_4^-$ was carried out directly. For SiO_2 films, a previous surface functionalization with amine groups was performed, to allow the Au precursor adsorption onto the surface [32]. The functionalization was carried out at room temperature by immersing the films for 20 h in a 2×10^{-4} mol·dm^{-3} APTES solution in ethanol, followed by a careful rinsing with the same solvent [33].

The Au loaded films were denominated according to the oxide, the template and the number of A/R cycles used to Au NPs load, as follows: ZrB-8C$_{Au}$, ZrF-8C$_{Au}$ and ZrF-15C$_{Au}$ for ZrO_2 films and SiB-8C$_{Au}$ and SiF-8C$_{Au}$ for SiO_2 films; where yC$_{Au}$ represents the number y of A/R cycles.

2.2.4. Characterization of the films

MTF pore ordering and Au loading was studied by field emission scanning electron microscopy (FESEM, Carl-Zeiss SUPRA 40 operated at 3 kV and using an in lens detector, CMA-FCEyN-UBA) and transmission electron microscopy (TEM, Philips CM 200 operating at 180 kV, GM-CAC-CNEA). Au NPs growth was also monitored using an HP8453 UV–vis spectrophotometer.

The X-ray reflectometry (XRR) studies, used to determine film thicknesses, porosities and Au loading, were performed on a PanAnalytical Empyrean X-Ray diffractometer. Cu Kα_α radiation (1.54 Å), incident angle of 1°, a divergence slit of 0.38 mm and a mask of 10 mm were used for the measurements. Films thicknesses (T) were obtained from the Kiessig fringes in the reflectogram [34], using Eq. (1) (valid when $\theta > 4$ critical angle, θ_c):

$$T = \frac{\lambda}{2\Delta(\sin\theta)} \tag{1}$$

where $\boldsymbol{\lambda}$ is the wavelength of the X-rays and Δ (sin θ) is the period of these oscillations.

Electronic densities (ρ_e) of the films were obtained from the reflectivity critical angle θ_c [35], using Eq. (2):

$$\rho_e = \frac{\pi}{\lambda^2 r_e}\theta_c^2 \tag{2}$$

where $r_e = 2.813 \times 10^{-6}$ nm is the electron's classical radius.

Taking into account Eq. (2), the films' porosity can be estimated from XRR data by measuring the change in the critical angle (and thus, in the thin film density) when the RH changes from <5% (*i.e.* the pores are full of air) to >90% (*i.e.* the pores are filled with water). For that purpose, XRR measurements were made with the films placed inside a chamber whose humidity was controlled by bubbling dry or wet air [36].

The increment in the film density at high RH values was considered only due to the water content in the pores. After this assumption, the water volume fraction (F_{H2O}) within the film was determined using Eq. (3):

$$F_{H2O}\frac{\boldsymbol{\rho_{film+H2O}} - \boldsymbol{\rho_{film}\rho_{H2O}}}{} \tag{3}$$

where $\rho_{film+H2O}$ is the water-filled film electronic density (obtained using θ_c measured at RH ≥ 90%), ρ_{film} is the empty film electronic density (obtained using θ_c measured at RH < 5%) and the ρ_{H2O} is the water electronic density. This F_{H2O} is equivalent to the accessible porosity of the material.

Same approach was used to determine the Au filling (gold volume fraction, F_{Au}) inside the pores, using Eq. (4):

$$F_{Au} = \frac{(\boldsymbol{\rho_{film+Au}}) - \boldsymbol{\rho_{film}\rho_{Au}}}{} \tag{4}$$

where $\rho_{film+Au}$ is the Au-filled film electronic density (measured at RH < 5%), ρ_{film} is the electronic density of empty mesoporous film and ρ_{Au} is the gold electronic density.

Au mass density (δ_m) within the films was calculated by using Eq. (5):

$$\delta_m = \frac{\boldsymbol{\rho_{Au}}}{\boldsymbol{N_A}}\frac{\boldsymbol{A_{Au}Z_{Au}}}{} \tag{5}$$

where ρ_{Au} is difference between $\rho_{film+Au}$ and ρ_{film}, N_A is Avogadro's number, Z_{Au} is Au atomic number and A_{Au} is Au atomic mass.

Finally, the accessible porosity after Au loading was calculated by measuring the change in the critical angle of Au loaded samples between low and high RH [36].

2.2.5. Electrochemical measurements

Electrochemical experiments were performed with a computer controlled potentiostat/galvanostat (AUTOLAB PGSTAT30, Eco Chemie). A conventional three-electrode cell with a Ag/AgCl (sat. KCl) reference electrode and a Pt wire counter electrode was used. To prepare the working electrode, each mesoporous film prepared onto ITO (size: 7 × 2.5 cm) was cut into three pieces of approximately 2 × 2 cm. Thus, each film was used to prepare three electrodes with the same characteristics.

The working electrode was electrically connected using a gold wire through a small section of the free ITO substrate. Before electrochemical measurements, all solutions were deoxygenated by argon bubbling for at least 30 min. The electrochemical determination of As (III) concentration was performed by cyclic voltammetry and differential pulse voltammetry. The voltammetry experiments were carried out on As (III) solutions prepared by dissolving sodium arsenite in phosphate buffer solution (0.1 M PBS, pH = 7). The same solution without arsenic was used as reference.

The Au NPs electroactive surface area was electrochemically determined by assuming 390 µC$^\bullet$ cm^{-2} for the reduction of a gold oxide monolayer of polycrystalline surface [37]. The voltammetric responses of the Au loaded films were determined over 0.0 to +1.2 V vs Ag/AgCl potential range.

3. Results and discussion

The mesoporous ZrO_2 thin films were prepared by dip coating using a sol–gel based EISA route, according to previously reported procedures [29]. The obtained thin films present a locally ordered mesoporous structure, as can be seen in Fig. 1a for ZrB and 1c for ZrF. The average pore size is 3.8 ± 0.9 nm for ZrB films and 7 ± 1 nm for ZrF films, while the interpore distances are 8.1 and 16.5 nm, respectively (determined from measurements performed in several electron microscopy images). The obtained values are in agreement with previously obtained results [29].

Au nanoparticles were incorporated within the mesopores through repetitive adsorption-reduction cycles, using $AuCl_4^-$ as metallic precursor and $NaBH_4$ as reductant. The obtained films present a pink color due to Localized Surface Plasmon Resonance (LSPR) of Au NPs [31], whose intensity depend on the amount of A/R cycles used. TEM image of ZrB-8C$_{Au}$ sample (Fig. 1b) shows the Au NPs obtained after 8 A/R cycles. The NPs exhibit a spherical shape and seem to be isolated from the TEM point of view. As TEM images are a 2D projection of a 3D sample, contact between particles stacked along the film thickness cannot be ruled out.

Au NPs with bigger size were obtained by using more A/R cycles, observing also agglomeration between them along consecutive pores (Fig. 1d). The obtained particles sizes are 4 ± 1, 5 ± 1, 24.3 ± 0.9 nm for ZrB-8C$_{Au}$, ZrF-8C$_{Au}$ and ZrF-15C$_{Au}$, respectively. In the last system, and as consequence of the bigger number of A/R cycles, the particles are larger than the pore size (see inset in Fig. 1d). This observation indicates that the TEM resolution does not allow distinguishing each particle separately and thus, the contact between them is ensured.

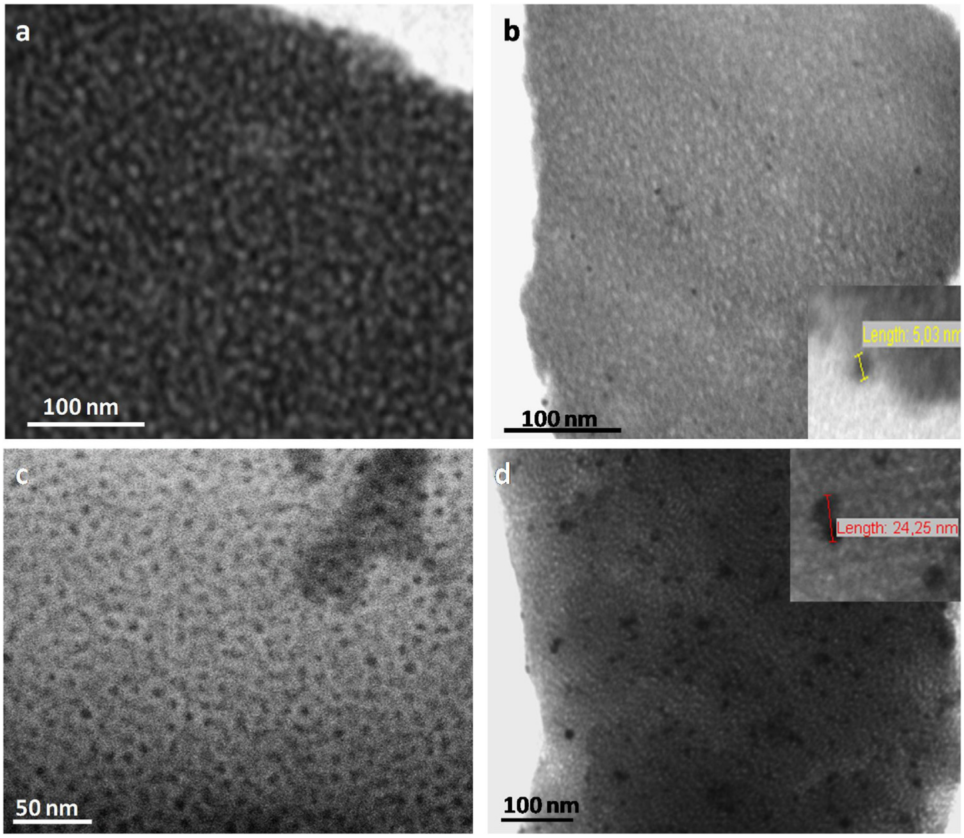

Fig. 1. TEM images of ZrB-8C$_{Au}$ sample with focus on the oxide's structure (a) and in the Au NPs included within (b), SEM image of ZrF sample surface (c) and TEM image of ZrF-15C$_{Au}$ sample (d).

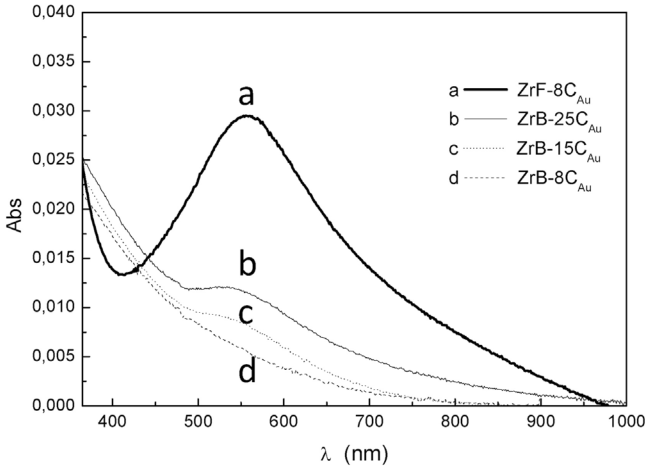

Fig. 2. UV–vis spectra of a) ZrF-8C$_{Au}$, b) ZrB-25C$_{Au}$, C) ZrB-15C$_{Au}$ and d) ZrB-8C$_{Au}$ samples.

Table 1
Thicknesses and porosities of ZrO$_2$ films.

System	Thickness/nm	Porosity/%
ZrF	90 ± 3	19 ± 1
ZrB	75 ± 3	21 ± 1

The obtained results also suggest that the pore diameter determines the NPs size only when less than 10 A/R cycles are used, greater A/R cycles number gives rise to NPs agglomeration visible by TEM.

The Au NPs loaded ZrO$_2$ films were characterized by UV–visible spectrometry, as can be seen in Fig. 2; optical images of selected samples are presented in Fig. S1 (Supplementary Material). A band centered around 550 nm attributed to the LSPR of Au NPs is clearly observed for ZrF-8C$_{Au}$ sample [8]. For Au NPs loaded ZrB, the band only appears when a higher amount of A/R cycles are performed. In fact, for ZrB-8C$_{Au}$ system the band is absent although the particles are present in the oxide, as demonstrated by electron microscopy images (Fig. 1b). This behavior can be explained taking into account the low Au NPs loading and the size of the particles (less than 5 nm diameter) [38]. When more A/R cycles are performed, more Au NPs are obtained and thus the band becomes clearly observable (see spectra b and c in Fig. 2). The intensity difference observed between the spectra of Au NPs included within ZrF and ZrB films can be attributed to the difference in the NPs diameters, according to Mie theory [39,40]. Moreover, the width of the absorption band indicates that at least some of the Au NPs are in contact between them [39].

ZrO$_2$ films thicknesses and porosities were obtained by XRR; selected obtained reflectograms are presented in Fig. 3.

An example of the oscillations due to the constructive interference of reflected X-rays on both thin film interfaces can be seen in Fig. 3a. From those oscillations, the thickness of the films was obtained using Eq. (1); the results are presented in Table 1.

Porosities were obtained from XRR patterns measured at low and high RH, using Eqs. (2)–(3). The obtained values, presented in Table 1, are in agreement with previously reported values [29].

Once the films were loaded with Au, two different parameters were evaluated with XRR: the NPs loading and the remaining accessible porosity. In Fig. 3b–d, changes in the θ_c are observed when comparing empty ZrO$_2$ films with Au NPs loaded ones. The phenomenon is a consequence of films' electronic density changes due

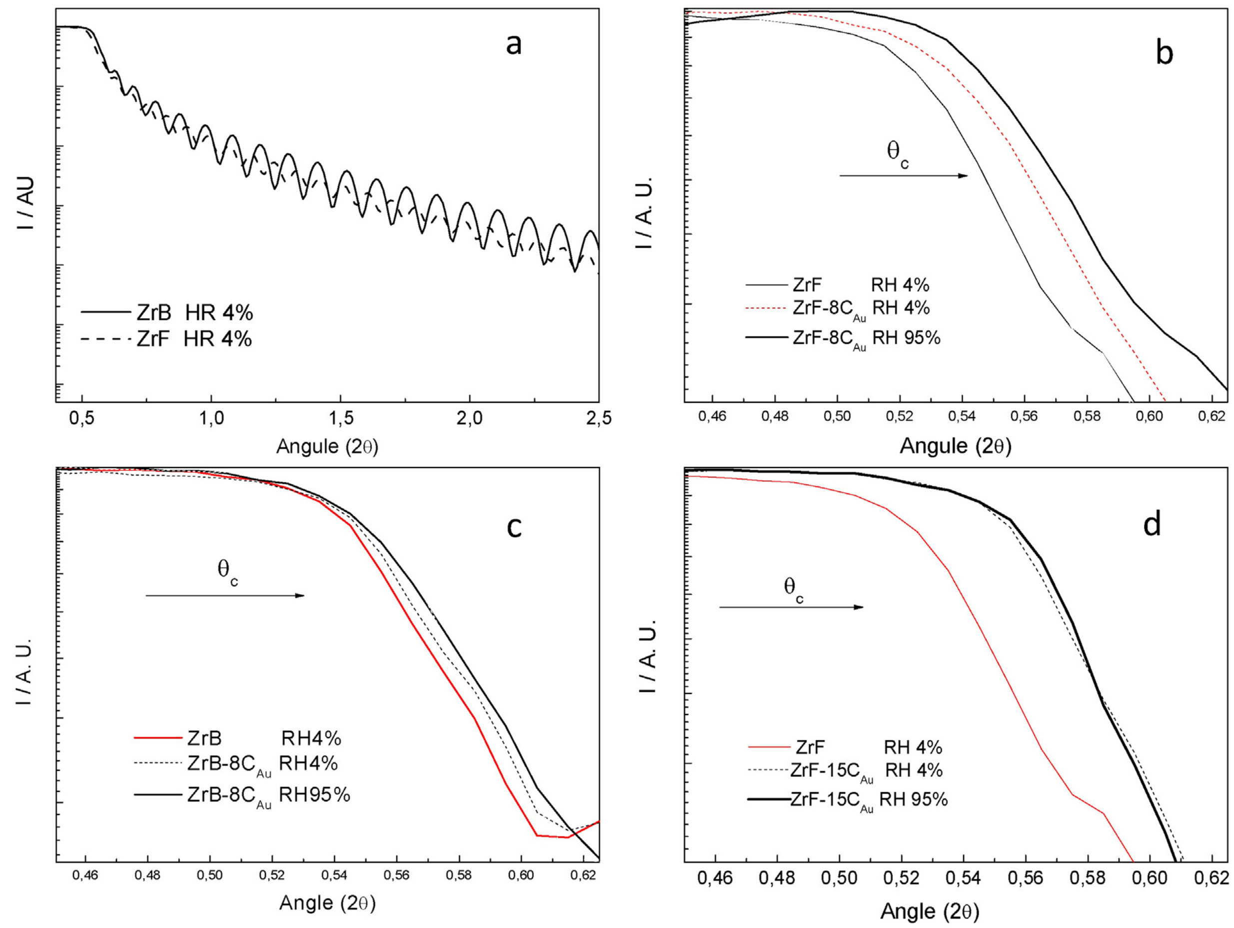

Fig. 3. XRR of a) ZrB and ZrB-8C_A, b) ZrF and ZrF-8C_{Au}, c) ZrB and ZrB-8C_{Au} and d) ZrF and ZrF-15C_{Au} measured at high (>90%) and low (<5%) RH, as indicated in the labels.

Table 2
F_{Au}, F_{H2O}, F_F, and Au mass density obtained from XRR measurements.

System	Au volume fraction (F_{Au})	Au filling factor (F_F) %	Au Mass density g·cm^{-3}	Water volume fraction (F_{H2O})
ZrF-15C_{Au}	0.12	35	0.455	0.4
ZrF-8C_{Au}	0.09	16	0.321	0.7
ZrB-8C_{Au}	0.08	15	0.329	0.5

to the formation of Au NPs inside the MTF [36]. The Au NPs loaded films were also measured at high (>90%) and low (<5%) RH. In this case, the XRR diagrams show a small shift in θ_c due to water condensation inside the pores. The obtained Au and water volume fractions calculated from θ_c shifts are presented in Table 2.

ZrF-8C_{Au} and ZrB-8C_{Au} samples present a similar Au filling fraction, while ZrF-15C_{Au} sample shows the highest value, indicating that an equivalent Au loading is obtained for systems with equal number of A/R cycles and different pore sizes.

Regarding the water volume fraction, the value for ZrF-8C_{Au} sample results higher than the ones obtained for ZrB-8C_{Au} and ZrF-15C_{Au} systems, indicating that a higher accessible porosity is available after Au NPs growth in this system. It is interesting to note that, although the Au loading is similar for ZrF-8C_{Au} and ZrB-8C_{Au} systems, there is a clear difference in the water volume fraction after Au NPs incorporation, indicating that the pore size plays a role in the final accessibility of the composite films. The number of A/R cycles also determines the final accessibility of the material, as can be observed when comparing the results for ZrF-15C_{Au} and ZrF-8C_{Au} samples. These results indicate that the composites' accessibility is determined both by the pore size and the number of A/R performed to load them.

3.1. Electrochemical measurements

The electrical wiring of Au NPs onto the film was corroborated by electrochemical experiments, measuring the modified electrodes in PBS at pH = 7. The Au NPs loaded MTF (ZrF-8C_{Au}, ZrF-15C_{Au} and ZrB-8C_{Au}) exhibit a sharp reduction peak at *ca.* 0.5 V, which is characteristic for the gold oxide reduction [41], as seen in Fig. 4a. A similar performance is observed for SiF-8C_{Au} and SiB-8C_{Au} systems (Fig. 4b).

Lowest currents are observed for SiF-8C_{Au} and SiB-8C_{Au} systems when compared with ZrF-8C_{Au} and ZrB-8C_{Au} films. This behavior is related to the lower gold load in the SiO_2 films when compared to ZrO_2 films, which is independently demonstrated by the lower absorbance observed in the UV- vis spectra of SiF-8C_{Au} sample, when compared with ZrF-8C_{Au} system (see Fig. S2).

The electroactive surface area of the Au NPs was calculated by measuring the area under the reduction peak [42] and assuming 390 μC·cm^{-2} for the charge passed per unit area on the surface of bulk Au. Table 3 shows the surface area values obtained for ZrO_2 systems; the results for SiO_2 samples are presented in Table S1.

ZrF-8C_{Au} presents the biggest electroactive area, even surpassing ZrF-15C_{Au}, which present the higher Au filling fraction

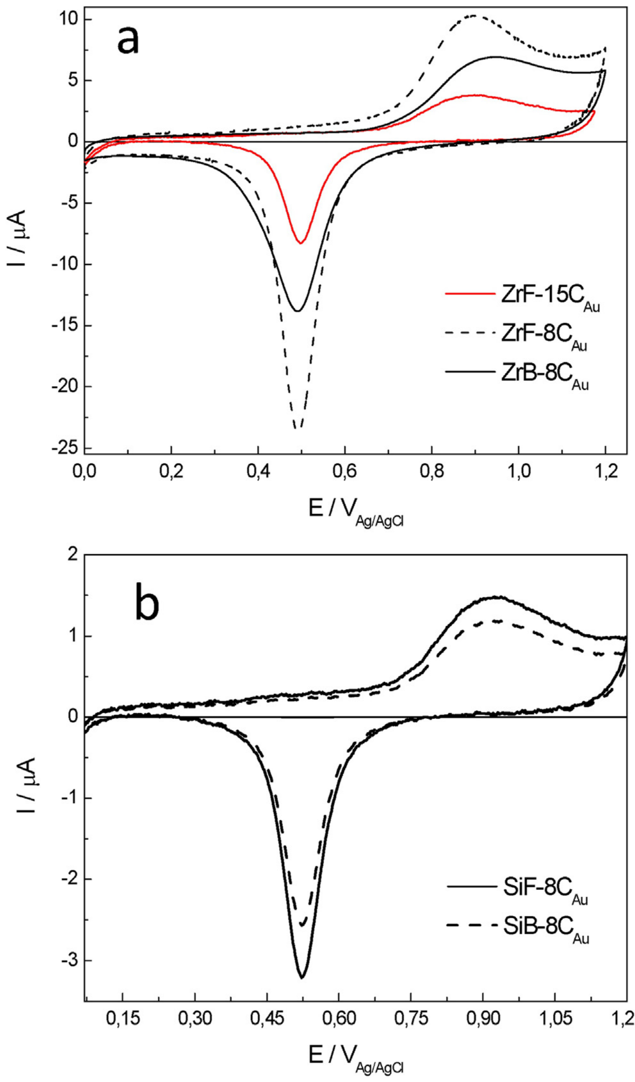

Fig. 4. Cyclic voltammograms of (a) ZrF-8C$_{Au}$, ZrF-15C$_{Au}$ and ZrB-8C$_{Au}$, (b) SiB-8C$_{Au}$ and SiF-8C$_{Au}$ electrodes in PBS pH = 7. Scan rate 10 mVs^{-1}.

Table 3
Surface area values obtained for the analyzed electrodes.

System	Gold electroactive area (cm^2) per cm^2 of electrode
ZrF-8C$_{Au}$	0.711
ZrB-8C$_{Au}$	0.590
ZrF-15C$_{Au}$	0.257

according to XRR measurements. This apparent contradiction can be explained taking into account the NPs agglomeration observed in the ZrF-15C$_{Au}$ system by TEM. As a consequence of such agglomeration, the Au exposed area is diminished and thus a smaller area is available for electrochemical reactions. In the same sense, ZrB-8C$_{Au}$ system shows the lowest electroactive area. This behavior can be related with pore blocking by Au NPs, which limits the electrolyte's accessibility. This behavior is in agreement with the accessible porosity results obtained by the XRR. Thus, ZrF-8C$_{Au}$ with bigger and thus harder to block pores (diameter around 7 nm instead of 3.8 nm) improves the accessible electrochemical surface area and the diffusion of electroactive species towards the Au NPs surface [43,44].

Lower electrochemical areas were obtained for SiF-8C$_{Au}$ and SiF-8C$_{Au}$ electrodes, due to the lower amount of Au incorporated in these systems. Therefore, in order to compare both oxide supports in the following experiments, the obtained currents were normalized for electrochemical area.

3.2. *Influence of Au amount on electrochemical response*

In order to evaluate the possible use of these composite materials as electrochemical sensors, cyclic voltammetry was employed to examine the electroanalytical performance as As (III) sensors. Arsenic (III) was chosen as a model analyte, since contamination with this ion is a worldwide problem and its concentration can be determined by electrochemical techniques. The experiments were carried out in PBS medium because arsenite is accompanied by a phosphate excess in natural waters, and the separation and detection of As(III) in the presence of phosphate usually represents a big challenge [45].

Fig. 5 shows the cyclic voltammograms of mesoporous ZrO$_2$ electrodes with and without Au NPs in the absence of As (III). As expected, redox peaks are not observed in the potential window of 0.15 – 0.65 V. However, a small increase in capacitive current is observed when Au NPs are incorporated within the film, since the particles increase the electroactive surface area.

Fig. 6 shows typical cyclic voltammetric responses in the range from 0.15–0.65 V for the different ZrO$_2$ electrodes in the presence of As (III). An oxidation peak is observed in all cases, caused by the oxidation of As (III) to As (V) [13,46]. This oxidation peak is not observed for the ZrF and ZrB electrodes, indicating that the As (III) oxidation is catalyzed by the Au NPs supported onto the films (see comparison of catalytic oxidation of As (III) in presence of different electrodes with and without Au NPs in Fig. S3) [47].

A shift in the potential of the current density peaks is observed in the CV when the different electrodes are compared [48,49]: 25 mV negative in ZrF-8C$_{Au}$ compared with ZrB-8C$_{Au}$ and 60 mV negative compared with ZrF-15C$_{Au}$. This behavior can be related with an alteration of the electroactive species diffusion coefficients within the mesoporous oxide in which the NPs are confined [50]. Also, the pore size and the occluded porosity play an important role in the electroactive species diffusion towards the catalyst, which is reflected in the displacement of the onset potential toward lower potential values. For example, ZrF-8C$_{Au}$ electrode shows bigger accessible porosity and lower oxidation potential in comparison with other electrodes (see Fig. 1 and Table 2). As a consequence, an apparent increase in the electron transfer kinetics appears, evidenced by the shift in the voltammetric I$_{peak}$ potential [48], however this shift could be related to the Au NPs size as reported by Han *et al.* [50–52]. These results suggest that ZrF-8C$_{Au}$ system has the best performance as electrode, achieving the highest current density and thus rendering a higher analytical sensibility for As (III) detection. Also for this electrode, a lower oxidation potential for As(III) to As(V) oxidation is required. This lower overpotential is desirable, since allows avoiding the interference of electro-oxidizable compounds that can appear at higher overpotentials [53–55].

On the other hand, the lowest current density oxidation peak for ZrF-15C$_{Au}$ could be attributed to the lower electroactive area in comparison with the others electrodes (see Table 2), related to the presence of inaccessible or agglomerated Au NPs (*i.e.* less available active surface).

3.3. *Influence of the support oxide on the electrochemical response*

In order to study the influence of the oxide used as support and its pore size, the electrochemical performance of Au NPs deposited onto SiO$_2$ and ZrO$_2$ MTF was compared. Fig. 7 shows the electro-oxidation of As (III) by SiF-8C$_{Au}$ and SiB-8C$_{Au}$ electrodes compared with ZrO$_2$ electrodes. The normalized peak currents densities

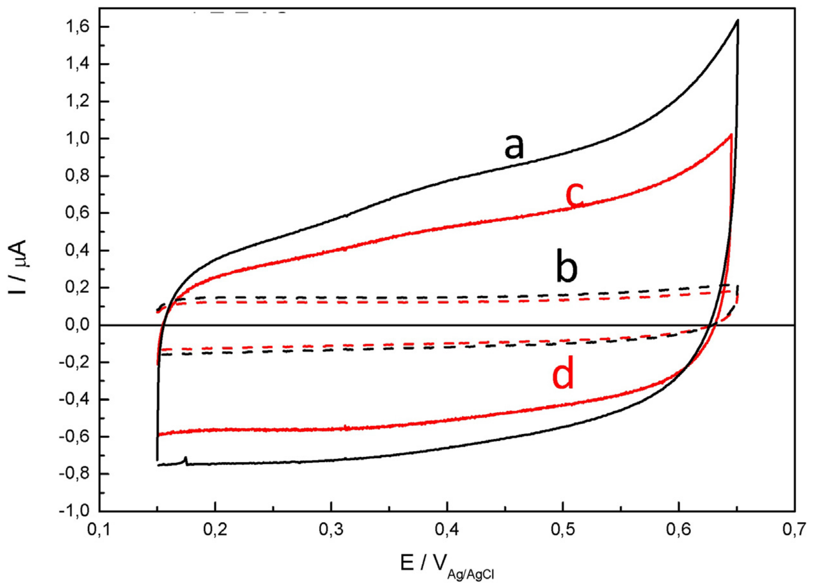

Fig. 5. Cyclic voltammograms of ZrF (b), ZrF-8C_{Au} (a), ZrB (d) and ZrB-8C_{Au} (c) electrodes in PBS pH = 7 without As (III). Scan rate 10 mVs^{-1}.

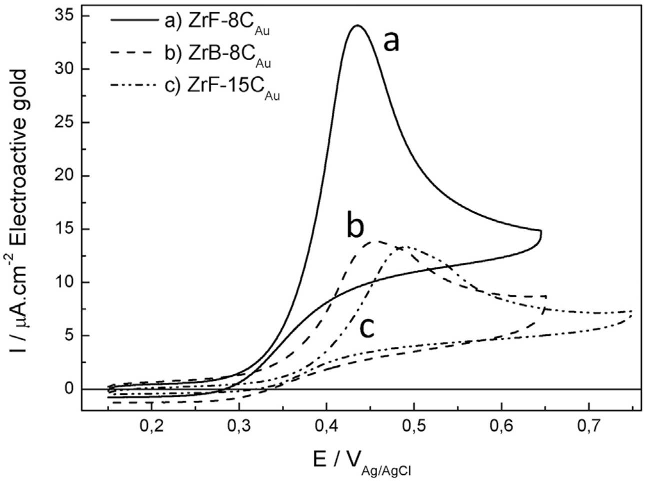

Fig. 6. CV of (a) ZrF-8C_{Au}, (b) ZrB-8C_{Au} and (c) ZrF-15C_{Au} systems in presence 360 μM As (III) solution – PBS pH = 7. Scan rate 10 mVs^{-1}.
Potential peaks: a) 0.430 V, b) 0.455 and c) 0.490 V vs Ag/AgCl.

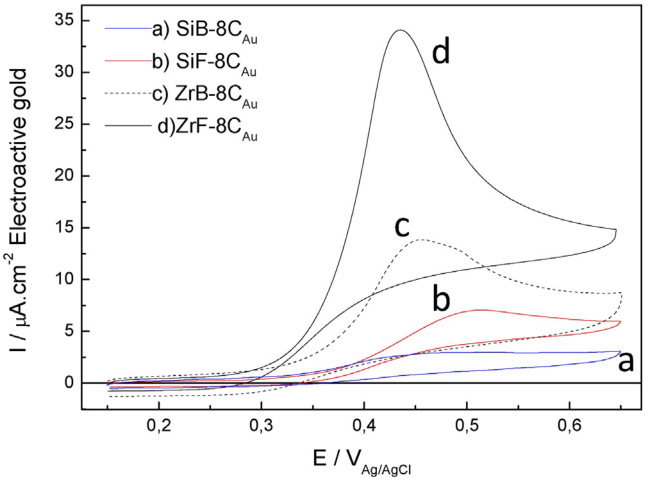

Fig. 7. Cyclic voltammograms of SiB-8C_{Au} (a), SiF-8C_{Au} (b), ZrB-8C_{Au} (c) and ZrF-8C_{Au} (d) in presence 360 μM As (III) solution in PBS pH = 7. Scan rate 10 mVs^{-1}.

obtained are 34.19 and 7.08 μA·cm^{-2} for ZrF-8C_{Au} and ZrB-8C_{Au}; and 7.05 and 2.92 μA·cm^{-2} SiF-8C_{Au} and SiB-8C_{Au}, respectively. These normalized currents clearly show that the pore size influences the electrochemical response of the electrodes: the SiF-8C_{Au} electrode (bigger pores) has a peak current 5 times higher than SiB-8C_{Au} electrode (smaller pores). Similar behavior is observed by comparing ZF-8C_{Au} and ZB-8C_{Au} electrodes. However, the type of oxide used as support has a major role in the electrode's performance: a clearly higher oxidation current is observed when ZrO_2 is used as support. This behavior can be explained taking into account that As (III) can be adsorbed onto ZrO_2 [23–25] and no evidence of such phenomenon has been reported for SiO_2. Thus, the combination of Au NPs and mesoporous ZrO_2 is more suitable for the As (III) detection than the equivalent systems prepared with SiO_2. In the first case, the analyte is adsorbed onto the ZrO_2 surface and it is subsequently oxidized by Au NPs allowing the improvement of the analytical sensibility, as was observed previously for similar systems [56–59].

3.4. *Quantitative determination of As (III)*

Taking the above presented results into consideration, the ZrF-8C_{Au} system was chosen for a preliminary test of electrocatalytic quantitative determination of As (III). This system showed the best electrochemical performance when compared to the other developed systems: the highest oxidation current and the lowest overpotential.

Using the ZrF-8C_{Au} electrode, the oxidation peak currents for different As (III) concentrations in the range 5–100 ppb were recorded by cyclic voltammetry and a linear response was obtained (Fig. 8). The electrochemical response was very reproducible; the presented data are an average of 3 independent experiments.

The obtained linear regression equation for the 5–100 ppb concentration range is: $I = 0.026$ [As (III)] + 0.76, with a correlation coefficient of 0.9973. The tested range was selected due to the interest in detecting low As (III) concentrations for analytical purposes. However, the CV response was linear in the 5 ppb to 0.7 ppm range. Interestingly, for higher As (III) concentrations (see for example the CV for 360 μM –27 ppm- concentration in Fig. 7), the relationship between peak intensity and concentration was lower than the one obtained for lower As (III) concentrations. This behavior has been observed previously [60] and could be related with a change in

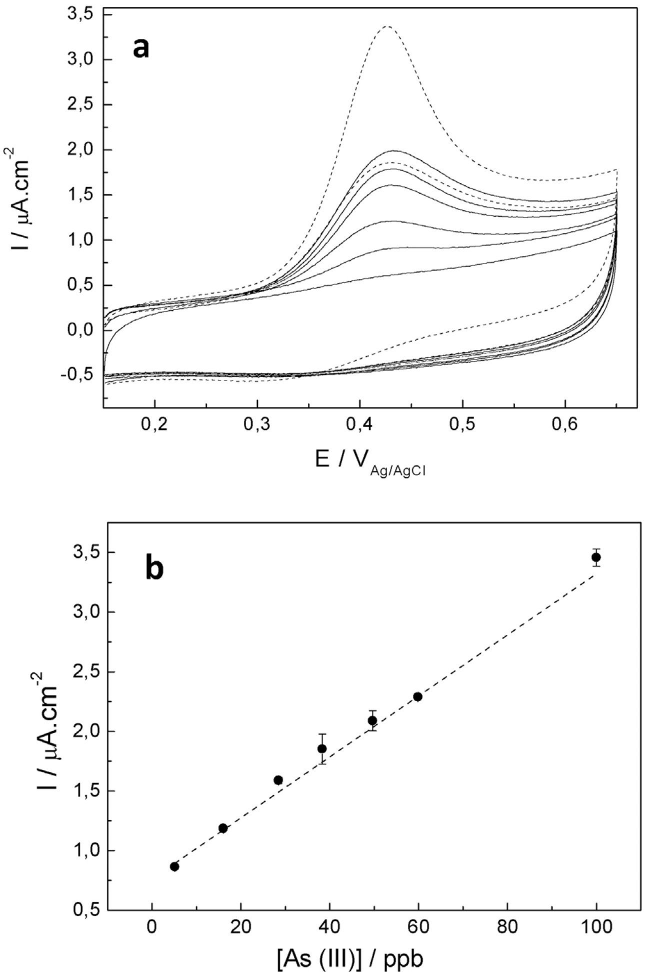

Fig. 8. (a) Cyclic voltammograms of ZrF-8C$_{Au}$ electrode with As (III) concentration of 5.0, 15.0, 30.0, 40.0, 50.0, 60.0 and 100.0 ppb in PBS pH = 7. Scan rate 10 mVs^{-1}. (b) Linear calibration plot for As (III) detection.

the way the analyte reaches the active part of the electrode, as a consequence of the system's saturation.

The theoretical detection limit (LOD) was estimated to be 1 ppb, calculated as three times the standard deviation of the blank's signal divided by the slope of the regression line [61]. This LOD is better than the one reported for Au NPs deposited onto ITO through CV (5.0 ppm) [21] indicating that ZrO$_2$ MTF improves the electrode performance for As (III) quantification. Furthermore, mesoporous structure acts as the NPs support, conferring a stable design to the electrode. Interestingly, the advantages of the ZrF-8C$_{Au}$ system are more notorious when compared with ZrB-8C$_{Au}$ system, which contains a similar amount of Au NPs but a smaller pore size and lower accessibility. For this case, the As (III) detection is only possible in the 1–5 ppm range (see Fig. S4).

The stability of ZrB-8C$_{Au}$ and ZrF-8C$_{Au}$ electrodes was evaluated by applying potentials more negative than 0.15 V, through CV. The electrode behavior was not affected by the applied negative potentials, as can be seen in Fig. S5.

The application of more negative potentials produces higher peak currents and improves the electrochemical sensing of As (III) (Fig. S6) [59]. These results suggest that the higher peak currents obtained could be related to enhanced As (III) adsorption onto the electrode, when negative potentials are applied [62]. Also, the synthesized electrodes were unaffected by the negative potentials applied; thus, more negative potential can be used on Au NPs modified electrodes, improving the sensor's response. A similar behavior was reported by Dai *et al.* [21] for Au NPs supported on ITO; this phenomenon is associated to the stability of electrodes due to highest oxidation currents obtained [59,63].

It is also important to note that since ZrO$_2$ is mechanically and chemically stable [8,29], and the Au NPs are stabilized inside the mesopores, the composite material results extremely stable over time. The presented electrodes were used in more than 20 electrochemical experiments each, without noticing any change in its performance.

Finally, it worth noting that the detection limit obtained in phosphate media (1.0 ppb) is suitable to perform drinking water analysis, taking into account that WHO maximum permissible limit (10 ppb) [41]. However, the results presented in this paper are preliminary and more experiments need to be done to ensure the usefulness of the developed electrodes in real samples, including detailed studies about possible interferences effects.

Moreover, if any particular application requires a lower detection limit, the sensitivity of these electrodes can be increased by using more complex electrochemical techniques such as square wave voltammetry or differential pulse voltammetry (DPV) [17] (see, as a preliminar example, Fig. S7: DPV on ZrF-8C$_{Au}$ and ZrB-8C$_{Au}$ electrodes).

4. Conclusions

A new family of electrodes prepared by Au NPs deposition onto mesoporous ZrO$_2$ was designed and developed, and its capability for As (III) determination in water was demonstrated.

By comparison with non loaded ZrO$_2$ MTF and Au loaded SiO$_2$ electrodes, it was possible to determine that the chosen design is ideal for the As (III) detection, since it combines the electrocatalytic behavior of Au NPs and the adsorption capacity of mesoporous ZrO$_2$. In fact, no signal was observed for ZrF and ZrB samples and a low electrochemical current was observed in the case of SiB-8C$_{Au}$ and SiF-8C$_{Au}$ samples.

Within the Au loaded ZrO$_2$ films, a clear difference in the electrochemical performance of the material was observed depending on the pore size and the amount of incorporated Au NPs. In particular, ZrF-8C$_{Au}$ presented the higher sensitivity when compared with samples with higher amount of Au but lower accessibility due to pore clogging (ZrF-15C$_{Au}$) and samples with similar Au loading and lower accessibility due to smaller pore size (ZrB-8C$_{Au}$). A detection limit as low as 1.0 ppb of As (III) was achieved with ZrF-8C$_{Au}$ electrodes, allowing the detection of this contaminant in relevant concentrations for water analysis and, notably, in the presence of phosphate (a usual interferent).

Thus, this work demonstrates the importance of a careful material design and characterization to improve the performance of mesoporous materials used as electrodes for electrochemical detection. Finally, it is important to note that the results presented here for As (III) detection can be expanded to the detection of other anions or cations, by simply changing the identity of the mesoporous framework and thus, its affinity for particular species.

Acknowledgements

The authors thank financial support from ANPCyT (PICT 2012-0111) and CONICET (PIP 2012-00044CO). R.C.R. acknowledges CONICET for a postdoctoral scholarship. M. C. Fuertes and M. M. Zalduendo are gratefully acknowledged for their assistance with XRR measurements and G. Zbihlei is acknowledged for TEM measurements.

Appendix A. Supplementary data

Supplementary data associated with this article can be found, in the online version, at http://dx.doi.org/10.1016/j.snb.2017.07.072.

References

[1] K. Saha, S.S. Agasti, C. Kim, X. Li, V.M. Rotello, Gold nanoparticles in chemical and biological sensing, Chem. Rev. 112 (2012) 2739–2779.
[2] A.N. Shipway, E. Katz, I. Willner, Nanoparticle arrays on surfaces for electronic, optical, and sensor applications, Chem. Phys. Chem. 1 (2000) 18–52.
[3] E. Dilonardo, M. Penza, M. Alvisi, C. Di Franco, R. Rossi, F. Palmisano, et al., Electrophoretic deposition of Au NPs on MWCNT-based gas sensor for tailored gas detection with enhanced sensing properties, Sens. Actuators B 223 (2016) 417–428.
[4] L. Fang, B. Liu, L. Liu, Y. Li, K. Huang, Q. Zhang, Direct electrochemistry of glucose oxidase immobilized on Au nanoparticles-functionalized 3D hierarchically ZnO nanostructures and its application to bioelectrochemical glucose sensor, Sens. Actuators B 222 (2016) 1096–1102.
[5] C.H. Kuo, W. Li, L. Pahalagedara, A.M. El-Sawy, D. Kriz, N. Genz, et al., Understanding the role of gold nanoparticles in enhancing the catalytic activity of manganese oxides in water oxidation reactions, Angew. Chem. Int. Ed. 54 (2015) 2345–2350.
[6] R. Sardar, A.M. Funston, P. Mulvaney, R.W. Murray, Gold nanoparticles: past, present, and future, Langmuir 25 (2009) 13840–13851.
[7] S. Guo, E. Wang, Synthesis and electrochemical applications of gold nanoparticles, Anal. Chim. Acta 598 (2007) 181–192.
[8] I.L. Violi, A. Zelcer, M.M. Bruno, V. Luca, G.J. Soler-Illia, Gold nanoparticles supported in Zirconia–Ceria Mesoporous thin films: a highly active reusable heterogeneous nanocatalyst, ACS Appl. Mater. Interfaces 7 (2015) 1114–1121.
[9] A. Walcarius, Mesoporous materials and electrochemistry, Chem. Soc. Rev. 42 (2013) 4098–4140.
[10] P. Innocenzi, L. Malfatti, Mesoporous thin films: properties and applications, Chem. Soc. Rev. 42 (2013) 4198–4216.
[11] M. Etienne, Y. Guillemin, D. Grosso, A. Walcarius, Electrochemical approaches for the fabrication and/or characterization of pure and hybrid templated mesoporous oxide thin films: a review, Anal. Bioanal. Chem. 405 (2013) 1497–1512.
[12] P.C. Angelomé, L.M. Liz-Marzán, Synthesis and applications of mesoporous nanocomposites containing metal nanoparticles, J. Sol. Gel. Sci. Technol. 70 (2014) 180–190.
[13] D. Kato, T. Kamata, D. Kato, H. Yanagisawa, O. Niwa, Au nanoparticle-embedded carbon films for electrochemical As3+ detection with high sensitivity and stability, Anal. Chem. 88 (2016) 2944–2951.
[14] Q. Sun, J. Chen, H. Zhang, S. Ding, Z. Li, P.N. Williams, et al., Improved diffusive gradients in thin films (DGT) measurement of total dissolved inorganic arsenic in waters and soils using a hydrous zirconium oxide binding layer, Anal. Chem. 86 (2014) 3060–3067.
[15] M.B. Gumpu, S. Sethuraman, U.M. Krishnan, J.B.B. Rayappan, A review on detection of heavy metal ions in water–an electrochemical approach, Sens. Actuators B 213 (2015) 515–533.
[16] D.Q. Hung, O. Nekrassova, R.G. Compton, Analytical methods for inorganic arsenic in water: a review, Talanta 64 (2004) 269–277.
[17] Z.-G. Liu, X.-J. Huang, Voltammetric determination of inorganic arsenic, TrAC Trends Anal. Chem. 60 (2014) 25–35.
[18] B.J. Sanghavi, N.S. Gadhari, P.K. Kalambate, S.P. Karna, A.K. Srivastava, Potentiometric stripping analysis of arsenic using a graphene paste electrode modified with a thiacrown ether and gold nanoparticles, Microchim. Acta 182 (2015) 1473–1481.
[19] E. Majid, S. Hrapovic, Y. Liu, K.B. Male, J.H. Luong, Electrochemical determination of arsenite using a gold nanoparticle modified glassy carbon electrode and flow analysis, Anal. Chem. 78 (2006) 762–769.
[20] C. Gao, X.-Y. Yu, S.-Q. Xiong, J.-H. Liu, X.-J. Huang, Electrochemical detection of arsenic (III) completely free from noble metal: fe3O4 microspheres-room temperature ionic liquid composite showing better performance than gold, Anal. Chem. 85 (2013) 2673–2680.
[21] X. Dai, R.G. Compton, Direct electrodeposition of gold nanoparticles onto indium tin oxide film coated glass: application to the detection of arsenic (III), Anal. Sci. 22 (2006) 567–570.
[22] J.-F. Huang, H.-H. Chen, Gold-nanoparticle-embedded nafion composite modified on glassy carbon electrode for highly selective detection of arsenic (III), Talanta 116 (2013) 852–859.
[23] H. Cui, Y. Su, Q. Li, S. Gao, J.K. Shang, Exceptional arsenic (III, V) removal performance of highly porous, nanostructured ZrO 2 spheres for fixed bed reactors and the full-scale system modeling, Water Res. 47 (2013) 6258–6268.
[24] H. Cui, Q. Li, S. Gao, J.K. Shang, Strong adsorption of arsenic species by amorphous zirconium oxide nanoparticles, J. Ind. Eng. Chem. 18 (2012) 1418–1427.
[25] J. Luo, X. Luo, C. Hu, J.C. Crittenden, J. Qu, Zirconia (ZrO2) embedded in carbon nanowires via electrospinning for efficient arsenic removal from water combined with DFT studies, ACS Appl. Mater. Interfaces 8 (2016) 18912–18921.
[26] S.A. Ntim, S. Mitra, Adsorption of arsenic on multiwall carbon nanotube–zirconia nanohybrid for potential drinking water purification, J. Colloid Interface Sci. 375 (2012) 154–159.
[27] C.J. Brinker, Y. Lu, A. Sellinger, H. Fan, Evaporation-induced self-assembly nanostructures made easy, Adv. Mater. 11 (1999) 579–585.
[28] M.D. Pérez, E. Otal, S.A. Bilmes, G.J. Soler-Illia, E.L. Crepaldi, D. Grosso, et al., Growth of gold nanoparticle arrays in TiO2 mesoporous matrixes, Langmuir 20 (2004) 6879–6886.
[29] A. Zelcer, G.J.A.A. Soler-Illia, One-step preparation of UV transparent highly ordered mesoporous zirconia thin films, J. Mater. Chem. C 1 (2013) 1359–1367.
[30] P.C. Angelomé, M.C. Fuertes, G.J. Soler-Illia, Multifunctional, multilayer, multiscale: integrative synthesis of complex macroporous and mesoporous thin films with spatial separation of porosity and function, Adv. Mater. 18 (2006) 2397–2402.
[31] V. Saínchez, E. Martínez, M. Martínez Ricci, H. Troiani, G. Soler-Illia, Optical properties of Au nanoparticles included in mesoporous TiO2 thin films: a dual experimental and modeling study, J. Phys. Chem. C 117 (2013) 7246–7259.
[32] A. Calvo, M.C. Fuertes, B. Yameen, F.J. Williams, O. Azzaroni, G.J.A.A. Soler-Illia, Nanochemistry in confined environments: polyelectrolyte brush-assisted synthesis of gold nanoparticles inside ordered mesoporous thin films, Langmuir 26 (2010) 5559–5567.
[33] A. Calvo, M. Joselevich, G.J. Soler-Illia, F.J. Williams, Chemical reactivity of amino-functionalized mesoporous silica thin films obtained by co-condensation and post-grafting routes, Microporous Mesoporous Mater. 121 (2009) 67–72.
[34] A. Gibaud, G. Vignaud, Specular reflectivity from smooth and rough surfaces, X-ray and Neutron Reflectivity, Springer (2009) 85–131.
[35] A. Van der Lee, Grazing incidence specular reflectivity: theory, experiment, and applications, Solid State Sci. 2 (2000) 257–278.
[36] M. Fuertes, M. Marchena, M. Marchi, A. Wolosiuk, G. Soler-Illia, Controlled deposition of silver nanoparticles in mesoporous single-or multilayer thin films: from tuned pore filling to selective spatial location of nanometric objects, Small 5 (2009) 272–280.
[37] R. Szamocki, A. Velichko, C. Holzapfel, F. Mücklich, S. Ravaine, P. Garrigue, et al., Macroporous ultramicroelectrodes for improved electroanalytical measurements, Anal. Chem. 79 (2007) 533–539.
[38] W. Haiss, N.T. Thanh, J. Aveyard, D.G. Fernig, Determination of size and concentration of gold nanoparticles from UV–vis spectra, Anal. Chem. 79 (2007) 4215–4221.
[39] U. Kreibig, M. Vollmer, Optical Properties of Metal Clusters, Springer, 1995.
[40] J. Piella, N.G. Bastús, V. Puntes, Size-controlled synthesis of sub-10-nanometer citrate-stabilized gold nanoparticles and related optical properties, Chem. Mater. 28 (2016) 1066–1075.
[41] X. Dai, R.G. Compton, Gold nanoparticle modified electrodes show a reduced interference by Cu (II) in the detection of As (III) using anodic stripping voltammetry, Electroanalysis 17 (2005) 1325–1330.
[42] S. Trasatti, O. Petrii, Real surface area measurements in electrochemistry, Pure Appl. Chem. 63 (1991) 711–734.
[43] J. Chmiola, G. Yushin, Y. Gogotsi, C. Portet, P. Simon, P.-L. Taberna, Anomalous increase in carbon capacitance at pore sizes less than 1 nanometer, Science 313 (2006) 1760–1763.
[44] M. Boota, K. Hatzell, M. Alhabeb, E. Kumbur, Y. Gogotsi, Graphene-containing flowable electrodes for capacitive energy storage, Carbon 92 (2015) 142–149.
[45] L. Rassaei, M. Sillanpää, R.W. French, R.G. Compton, F. Marken, Arsenite determination in phosphate media at electroaggregated gold nanoparticle deposits, Electroanalysis 20 (2008) 1286–1292.
[46] M. Yang, X. Chen, T.-J. Jiang, Z. Guo, J.-H. Liu, X.-J. Huang, Electrochemical detection of trace arsenic (III) by nanocomposite of nanorod-Like α-MnO2 decorated with ∼5 nm Au nanoparticles: considering the change of arsenic speciation, Anal. Chem. 88 (2016) 9720–9728.
[47] G. Bhanjana, N. Dilbaghi, S. Chaudhary, K.-H. Kim, S. Kumar, Robust and direct electrochemical sensing of arsenic using zirconia nanocubes, Analyst 141 (13) (2016) 4211–4218.
[48] J. Masa, C. Batchelor-McAuley, W. Schuhmann, R.G. Compton, Koutecky-Levich analysis applied to nanoparticle modified rotating disk electrodes: electrocatalysis or misinterpretation, Nano Res. 7 (2014) 71–78.
[49] K.R. Ward, R.G. Compton, Quantifying the apparent 'Catalytic'effect of porous electrode surfaces, J. Electroanal. Chem. 724 (2014) 43–47.
[50] W.G. Hepburn, C. Batchelor-McAuley, K. Tschulik, E.O. Barnes, R.T. Kachoosangi, R.G. Compton, Diffusional transport to and through thin-layer nanoparticle film modified electrodes: capped CdSe nanoparticle modified electrodes, Phys. Chem. Chem. Phys. 16 (2014) 18034–18041.
[51] S.E. Kleijn, S. Lai, M. Koper, P.R. Unwin, Electrochemistry of nanoparticles, Angew. Chem. Int. Ed. 53 (2014) 3558–3586.
[52] D. Han, S.-S. Kim, Y.-R. Kim, B.-H. Sohn, T.D. Chung, Surface coverage and size effects on electrochemical oxidation of uniform gold nanoparticles, Electrochem. Commun. 53 (2015) 11–14.
[53] P.K. Rastogi, D.K. Yadav, S. Pandey, V. Ganesan, P.K. Sonkar, R. Gupta, Synthesis and characterization of gold nanoparticles incorporated bentonite clay for electrocatalytic sensing of arsenic (III), J. Chem. Sci. 128 (2016) 349–356.
[54] C. Wang, X. Liu, J.P. Chen, K. Li, Superior removal of arsenic from water with zirconium metal-organic framework UiO-66, Sci. Rep. 5 (2015).
[55] R. Rajaram, S. Anandhakumar, J. Mathiyarasu, Electrocatalytic oxidation of NADH at low overpotential using nanoporous poly (3,

4)-ethylenedioxythiophene modified glassy carbon electrode, J. Electroanal. Chem. 746 (2015) 75–81.

[56] Y. Deng, Y. Cai, Z. Sun, J. Liu, C. Liu, J. Wei, et al., Multifunctional mesoporous composite microspheres with well-designed nanostructure: a highly integrated catalyst system, J. Am. Chem. Soc. 132 (2010) 8466–8473.

[57] E. Toral-Sanchez, J.R. Rangel-Mendez, L.F. Chazaro-Ruiz, Characterization of iron-modified carbon paste electrodes and their application in As (V) detection, J. Appl. Electrochem. 46 (2016) 205–215.

[58] L. Cui, J. Wu, H. Ju, Label-free signal-on aptasensor for sensitive electrochemical detection of arsenite, Biosens. Bioelectron. 79 (2016) 861–865.

[59] L. Bu, T. Gu, Y. Ma, C. Chen, Y. Tan, Q. Xie, et al., Enhanced cathodic preconcentration of as (0) at Au and Pt electrodes for anodic stripping voltammetry analysis of as (III) and As (V), J. Phys. Chem. C 119 (2015) 11400–11409.

[60] P.C.D. Toro, F.J. Arévalo, M.A. Zon, H. Fernández, Studies of the electrochemical behavior of moniliformin mycotoxin and its sensitive determination at pretreated glassy carbon electrodes in a non-aqueous medium, J. Electroanal. Chem. 738 (2015) 40–46.

[61] G. Krepper, G.D. Pierini, M.F. Pistonesi, M.S. Di Nezio, In-situ antimony film electrode for the determination of tetracyclines in Argentinean honey samples, Sens. Actuators B 241 (2017) 560–566.

[62] L. Bu, J. Liu, Q. Xie, S. Yao, Anodic stripping voltammetric analysis of trace arsenic (III) enhanced by mild hydrogen-evolution at a bimetallic Au–Pt nanoparticle modified glassy carbon electrode, Electrochem. Commun. 59 (2015) 28–31.

[63] P. Singh, K. Chauhan, V. Priya, R.K. Singhal, A greener approach for impressive removal of As (III)/As (V) from an ultra-low concentration using a highly efficient chitosan thiomer as a new adsorbent, RSC Adv. 6 (2016) 64946–64961.